Nanoscale

High-Yield Fabrication of Electromechanical Devices Based on Suspended Ti3C2Tx MXene Monolayers

Journal:	*Nanoscale*
Manuscript ID	NR-ART-10-2022-005493.R1
Article Type:	Paper
Date Submitted by the Author:	24-Nov-2022
Complete List of Authors:	Bagheri, Saman; University of Nebraska-Lincoln, Chemistry Abourahma, Jehad; University of Nebraska-Lincoln, Chemistry Lu, Haidong; University of Nebraska-Lincoln, Physics and Astronomy Vorobeva, Natalia; University of Nebraska-Lincoln, Chemistry Luo, Shengyuan; University of Nebraska-Lincoln, Chemistry Gruverman, Alexei; University of Nebraska-Lincoln, Department of Physics & Astronomy Sinitskii, Alexander; University of Nebraska-Lincoln, Chemistry

SCHOLARONE™
Manuscripts

High-Yield Fabrication of Electromechanical Devices Based on Suspended $Ti_3C_2T_x$ MXene Monolayers

Saman Bagheri,[1†] Jehad Abourahma,[1†] Haidong Lu,[2] Nataliia S. Vorobeva,[1] Shengyuan Luo,[1] Alexei Gruverman,[2,3] and Alexander Sinitskii[1,3,*]

[1]Department of Chemistry, University of Nebraska-Lincoln, Lincoln, NE 68588, USA

[2]Department of Physics and Astronomy, University of Nebraska, Lincoln, NE 68588, USA

[3]Nebraska Center for Materials and Nanoscience, University of Nebraska-Lincoln, Lincoln, NE 68588, USA

*E-mail: sinitskii@unl.edu

[†]These authors contributed equally to this work.

Keywords: 2D materials, MXene, titanium carbide, $Ti_3C_2T_x$, nanoelectromechanical systems, NEMS, electromechanical resonators

Abstract

MXenes, two-dimensional transition metal carbides, nitrides, and carbonitrides, are known for their exceptional electronic and mechanical properties. Yet, the experimental efforts toward the realization of MXene-based nanoelectromechanical systems (NEMS) combining electrical and mechanical functionalities of MXenes at the nanoscale remain very limited. Here, we demonstrate a high-yield fabrication of the electromechanical devices based on individual suspended monolayer MXene flakes. We employed $Ti_3C_2T_x$, the most popular MXene material to date, that can be produced as high-quality micrometer-scale monolayer flakes with a high electrical conductivity of over 10,000 S cm^{-1} and a high effective Young's modulus of about 330 GPa. These $Ti_3C_2T_x$ flakes can be transferred over prefabricated trenches in a Si/Si_3N_4 substrate at a high yield, potentially enabling fabrication of hundreds of electromechanical devices based on suspended MXene monolayers. We demonstrate very clean, uniform, and well-stretched membranes with different dimensions, with $Ti_3C_2T_x$ flakes suspended over trenches with gaps ranging from 200 nm to 2 μm. The resulting $Ti_3C_2T_x$ monolayer membranes were electrostatically actuated, while their vertical displacement was monitored using a tip of an atomic force microscope (AFM). The devices reliably responded to the electrostatic actuation in ambient conditions over multiple cycles and with different measurement parameters, such as AC frequency, AC voltage amplitude, and AFM tip loading force. The demonstration of the high-yield fabrication of working electromechanical devices based on suspended $Ti_3C_2T_x$ MXene membranes at the ultimate monolayer limit paves the way for the future exploration of the potential of MXenes for NEMS applications.

1. Introduction

Two-dimensional (2D) materials are widely recognized for their promise for nanoelectromechanical system (NEMS) applications.[1-3] Some 2D materials are known for their exceptionally high Young's moduli, particularly graphene (~1 TPa)[4] and hexagonal boron nitride (~870 GPa),[5] as well as their high chemical stability. Furthermore, because of their small thickness, especially in the monolayer limit, 2D membranes offer an extremely small mass and large surface area, both of which are highly advantageous for NEMS-based sensing applications. However, while 2D materials offer many attractive properties for nanoscale resonators, actuators, and other NEMS devices, their fabrication remains challenging because it typically involves delicate handling of micrometer-scale flakes that often need to be precisely transferred over prefabricated trenches or wells and suspended as well-stretched membranes without tearing, folding, and sagging. Because of these fabrication challenges, the successful experimental demonstrations of electromechanical resonators and actuators based on suspended monolayers remain fairly limited compared to plentiful examples of electronic devices based on 2D materials on solid substrates.[6] Some of the 2D materials that have been processed into electrostatically actuated monolayer and few-layer membranes include graphene,[7, 8] hexagonal boron nitride,[9] MoS_2,[10] $MoSe_2$,[11] WSe_2,[12] phosphorene,[13] as well as several van der Waals heterostructures.[14-16]

MXenes are a large class of 2D materials that have a great combination of properties for electromechanically controlled monolayer membranes and NEMS applications in general. First, MXenes are known for a great chemical diversity as a very large family of 2D carbides, nitrides, and carbonitrides with a general formula of $M_{n+1}X_nT_x$, where M is a transition metal, such as Ti, Nb, V, Cr, etc., X is carbon and/or nitrogen, n = 1, 2, 3, 4, or 5, and T_x represents the surface functional groups.[17-19] More than 30 different MXenes have been demonstrated experimentally,

and many others have been predicted theoretically.[17] Second, long before MXenes were discovered as a new family of 2D materials,[20] bulk transition metal carbides had already been known for their exceptional mechanical properties.[21] For example, an unfunctionalized monolayer of $Ti_3C_2T_x$, which is the most popular MXene material to date,[17] can be viewed as a (111) slab of a cubic TiC crystal,[22] for which the Young's modulus was measured to be 400 GPa.[23] When such $Ti_3C_2T_x$ sheets are experimentally produced as 2D MXenes, they have similar mechanical properties to cubic TiC, their bulk counterpart. Our nanoindentation measurements of $Ti_3C_2T_x$ MXene monolayers revealed their effective Young's modulus of about 330 GPa,[24] which is close to bulk TiC. Another monolayer MXene material, $Nb_4C_3T_x$, was shown to have an even higher effective Young's modulus of about 386 GPa, which is also comparable to the values reported for bulk NbC.[22] Many other MXene materials that have not been experimentally tested yet are also expected to have very high Young's moduli based on the values known for their bulk carbide counterparts. Third, MXenes are also known for their high electrical conductivity, which was also tested on individual monolayers and found to be over 1,000 S cm^{-1} for $Nb_4C_3T_x$[22, 25] and over 10,000 S cm^{-1} for $Ti_3C_2T_x$.[26] Finally, electrical and Raman measurements demonstrate that dried $Ti_3C_2T_x$ MXene flakes could be chemically stable on a time scale of multiple days,[27, 28] enabling the characterization of $Ti_3C_2T_x$ devices in ambient conditions.

Despite all these very attractive properties of MXenes for NEMS applications, experimental studies in this area remain very limited, which can be largely attributed to the fabrication challenges with the preparation of suspended MXene monolayers. Unlike flakes of many other 2D materials, such as graphene and MoS_2, that can be prepared in sizes of tens of micrometers directly on a substrate either by mechanical exfoliation[29, 30] or chemical vapor deposition,[31] MXene are synthesized in solution as relatively small flakes with typical lateral sizes

of only a few micrometers. Precise positioning of these small flakes over prefabricated indentations on a surface as well as preventing the solvent from sagging or tearing the suspended MXene monolayers during the evaporation, are not trivial tasks.[24] There are currently only three reports on suspended MXene monolayers, all of which employed the variations of the polydimethylsiloxane (PDMS) stamp-assisted transfer method and produced monolayer membranes suspended over circular wells.[22, 24, 32] From the fabrication standpoint, this is the most robust geometry, because in this case the suspended flake is supported from all sides. However, studies on other 2D materials often utilized other geometries that are still to be realized with MXenes – for example, graphene flakes suspended over trenches were widely utilized in many studies on intrinsic charge carrier mobilities,[33, 34] thermal conductivity,[35] controlled rippling,[36] electromechanical resonators,[7] and other topics.

In this study, we used $Ti_3C_2T_x$, the most popular MXene material,[17] and demonstrate a high-yield fabrication of electromechanical devices based on suspended monolayer flakes. With recent advances in increasing the average flake size of MXenes[37] and important optimizations of the PDMS-based flake transfer procedure that we report in this paper, it is possible to produce hundreds of electromechanical devices based on suspended MXene monolayers on a single substrate. In order to demonstrate the generality of this approach for devices with different geometries, we did not repeat the previously reported circular nanodrums,[22, 24, 32] and instead fabricated $Ti_3C_2T_x$ flakes suspended over trenches with different gaps ranging from 200 nm to 2 μm. Furthermore, we show that the produced electromechanical devices are operational, and the suspended flakes can actuate in response to an electric field, which is due to the combination of great mechanical and electrical properties of $Ti_3C_2T_x$ MXene. The mechanical characteristics of MXenes enable the fabrication of suspended membranes that are stable and could be elastically

deformed, while their high electrical conductivity means that they could be directly biased for electrostatic actuation. In a typical measurement, we applied a low-frequency AC potential difference between a suspended MXene monolayer and a substrate and recorded the vertical deflection of a membrane using atomic force microscopy (AFM). The monolayer $Ti_3C_2T_x$ membranes could be reliably actuated over multiple cycles in ambient conditions. This study demonstrates the feasibility of the high-yield fabrication of operational devices based on suspended MXene monolayers and paves the way for future studies of MXene-based NEMS structures and their advanced applications.

2. Results and discussion

$Ti_3C_2T_x$ MXene that we used in this study is schematically shown in the inset in Figure 1a. The scheme demonstrates the close-packed layers of titanium atoms with octahedral voids occupied by carbon atoms,[22] and also shows the functional groups (T_x), such as -OH, =O, and -F, which are present on the surface of solution-synthesized MXene flakes.[38, 39] $Ti_3C_2T_x$ MXene was synthesized by solution etching of Ti_3AlC_2 MAX phase using the minimally intensive layer delamination (MILD) method with some modifications;[27] see the detailed procedure in the Experimental section. Following the recent report by Shekhirev, *et al*., we delaminated the etching product into MXene sheets by very mild shaking, which was shown to increase the average flake size compared to the sonication-assisted exfoliation.[37]

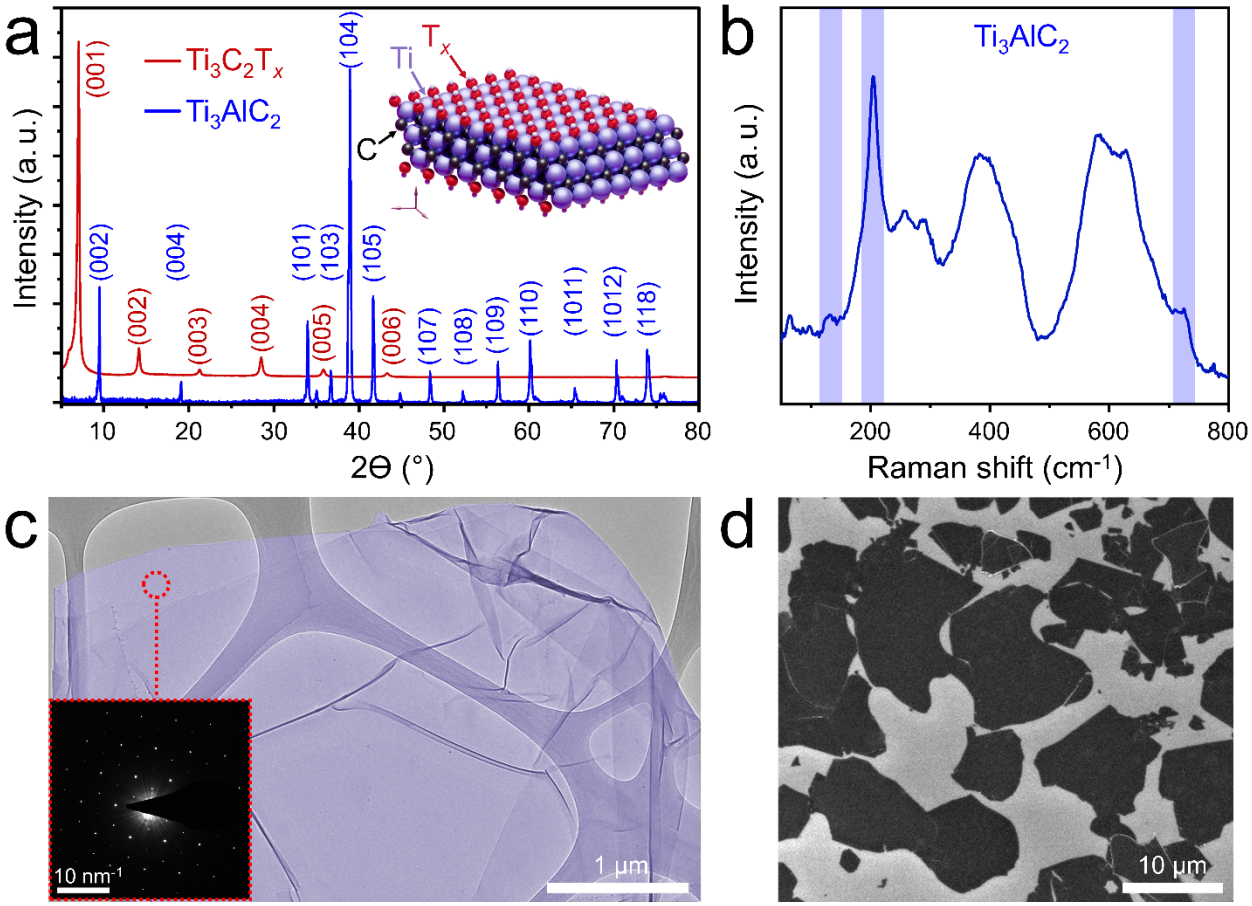

Figure 1. Materials characterization of $Ti_3C_2T_x$ MXene flakes. (a) XRD patterns of Ti_3AlC_2 MAX phase (blue) and a film of $Ti_3C_2T_x$ MXene flakes (red). The structure of a monolayer $Ti_3C_2T_x$ flake is shown in the inset. The surface T_x functional groups are schematically shown as hydroxyls, although other moieties, such as =O and -F, can also be present on the surface of MXene flakes.[38, 39] (b) Raman spectrum of $Ti_3C_2T_x$ MXene. The vertical blue lines highlight some of the characteristic Raman peaks of $Ti_3C_2T_x$ that are discussed in the text. (c) TEM image of a folded $Ti_3C_2T_x$ MXene flake on a lacey carbon grid. The flake is highlighted in blue for clarity. The inset shows a SAED pattern recorded from this flake. (d) SEM image of $Ti_3C_2T_x$ MXene flakes on a Si/SiO_2 substrate. Some flakes have lateral dimensions exceeding 10 μm.

Figure 1 summarizes the results of the materials characterization of $Ti_3C_2T_x$ MXene. Figure 1a shows X-ray diffraction (XRD) patterns of a powder of the precursor Ti_3AlC_2 MAX phase and a film of $Ti_3C_2T_x$ MXene flakes. The XRD pattern of the parent MAX phase (blue) is consistent with the literature and shows a high phase purity.[40] The XRD pattern of the $Ti_3C_2T_x$ MXene film shows no Ti_3AlC_2 peaks, implying that there are no MAX phase residues in significant amounts in the synthesized MXene. Sequences of 00*l* (*l* = 1, 2, ... 6) reflections are the only diffraction peaks in the red XRD pattern, suggesting a layered structure of a $Ti_3C_2T_x$ film with an interplanar spacing between the stacked MXene flakes of about 1.25 nm.[26]

A Raman spectrum of $Ti_3C_2T_x$ MXene flakes on a gold-coated Si/SiO_2 substrate was measured using a 532 nm excitation laser and is shown in Figure 1b. $Ti_3C_2T_x$ MXene was shown to have three main Raman peaks,[41] which are highlighted by the vertical blue lines in Figure 1b. The first peak at 128 cm^{-1} is a resonant Raman band, which is strongly enhanced when the laser energy is coupled with the plasmon resonance of $Ti_3C_2T_x$.[42] Here, because the excitation laser wavelength (532 nm) was substantially different from the spectral position of the plasmon resonance of $Ti_3C_2T_x$ between 700 and 800 nm,[42] this peak is barely visible in the Raman spectrum in Figure 1b. The other highlighted peaks at about 208 and 726 cm^{-1} correspond to the out-of-plane A_{1g} vibrations of the entire $Ti_3C_2T_x$ MXene flakes and carbon atoms, respectively.[28, 41] The broad peaks in the range from 230 to 470 cm^{-1} represent the vibrations of the surface functional groups of $Ti_3C_2T_x$ MXene, while the peaks in the range from 580 to 730 cm^{-1} represent the carbon vibrations.[41] The spectrum in Figure 1b is consistent with the previous reports on Raman spectroscopy of $Ti_3C_2T_x$ MXene[28, 41-43] and does not match the Raman spectrum of Ti_3AlC_2,[44] indicating that the precursor MAX phase was transformed into $Ti_3C_2T_x$ MXene.

The electron microscopy characterization of the $Ti_3C_2T_x$ is presented in Figure 1c,d. Figure 1c shows a TEM image of a folded $Ti_3C_2T_x$ MXene flake on a lacey carbon grid. The flake is several μm in size and has a very uniform surface. It should be noted that when $Ti_3C_2T_x$ flakes are partially oxidized, TEM investigation reveals pinhole defects and elongated TiO_2 particles,[45] none of which were observed in this case, indicating the high quality of the synthesized MXene material. The SAED pattern of the same flake (see the inset in Figure 1c) shows a hexagonal diffraction pattern, which is consistent with the structure of $Ti_3C_2T_x$ MXene (Figure 1a, inset) and confirms its high crystallinity.

As we outlined in the Introduction, for a high-yield fabrication of $Ti_3C_2T_x$ membranes, it is highly preferable to have large MXene flakes that could be conveniently suspended over prefabricated trenches in substrates and have a large area contact with a surface for strong adhesion. Such large flakes require gentle exfoliation of the products of MAX phase etching, as sonication or vigorous shaking of a MXene solution was previously shown to greatly reduce the average flake size.[27] For example, the original synthesis of $Ti_3C_2T_x$ employed an extensive sonication of the acid-etched Ti_3AlC_2 MAX phase, and the resulting MXene flakes mostly had sub-micrometer sizes.[20] Later research resulted in the MILD method, in which the etched product was not sonicated, and the resulting MXene flakes were considerably larger, in the several μm range.[27] A recent study further advanced the synthesis of ultralarge MXene flakes,[37] demonstrating that by further minimizing the shaking of the etching product, it is possible to produce of $Ti_3C_2T_x$ monolayers of up to 40 μm in lateral size. In this work, we used the conclusions of this approach as a guidance to produce large flakes of $Ti_3C_2T_x$, avoiding any unnecessary agitation of a MXene solution as well as high-speed centrifugation. For washing $Ti_3C_2T_x$ MXene from the unreacted LiF, we simply diluted the aqueous solution of the etched product with deionized water and left it

undisturbed for 1 h. The supernatant was gently decanted after the precipitation of multilayer MXenes. The multilayer MXenes gradually delaminated into thinner flakes as this technique was performed multiple times. The resulting MXene flakes with significant lateral dimensions could be isolated from bulk particles by centrifugation at 500 rpm. This gentle delamination yielded multiple uniform monolayer $Ti_3C_2T_x$ flakes with sizes exceeding 10 μm, as can be seen in the representative SEM image in Figure 1d.

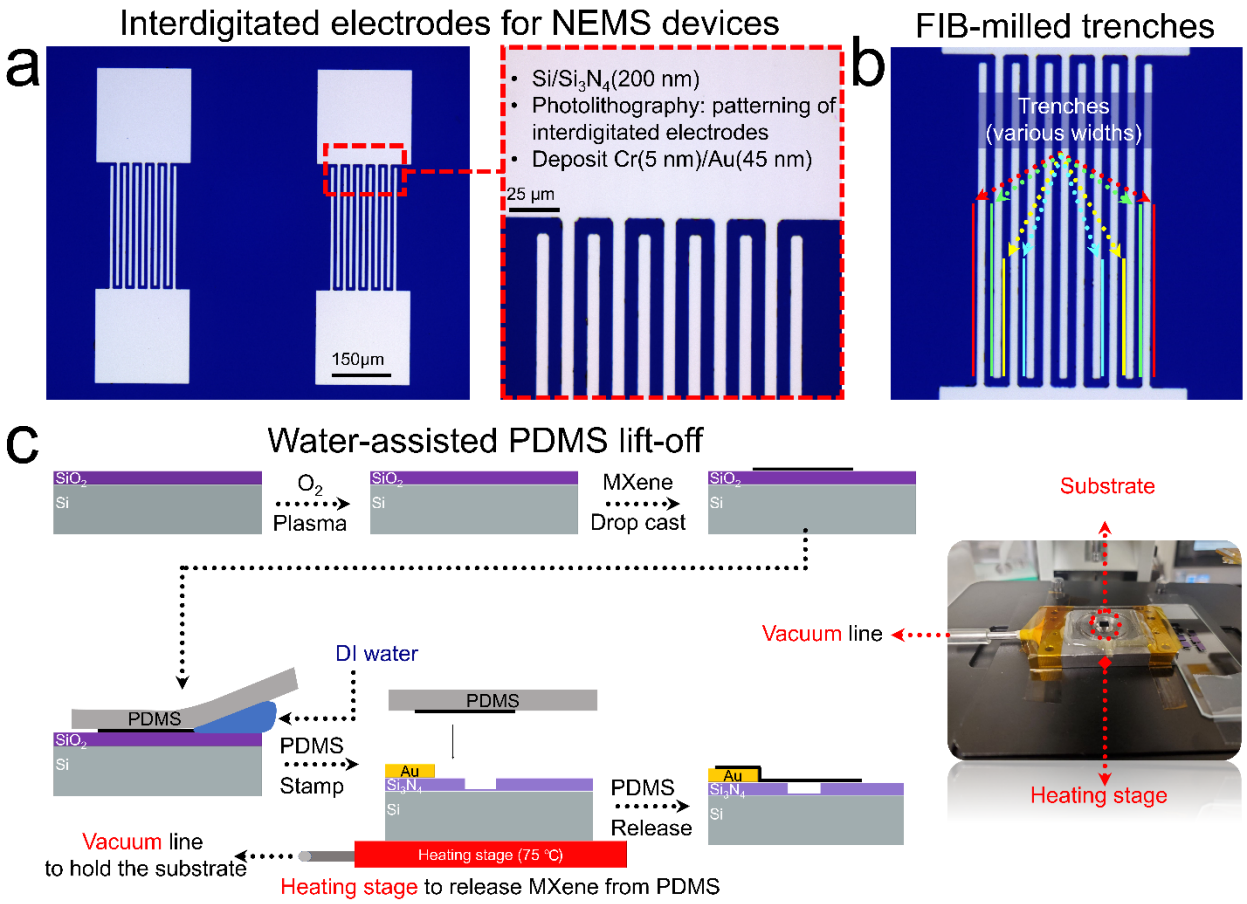

Figure 2. Water-assisted PDMS transfer of $Ti_3C_2T_x$ MXene flakes. (a) Optical photograph of two pairs of interdigitated Cr/Au electrodes on a Si/Si_3N_4 substrate. (b) Representative positions of the trenches with various widths that were milled in a Si/Si_3N_4 substrate near the Cr/Au electrodes by FIB. The trenches are highlighted by the colored lines for clarity. (c) Scheme of the transfer process. The inset shows optical photograph of a homebuilt transfer setup and heating stage.

Figure 2 shows the procedure that we used for the high-yield fabrication of electromechanical devices based on suspended MXene monolayers. First, we used photolithography to fabricate several pairs of Cr/Au interdigitated electrodes on a Si/Si_3N_4 substrate; two of these pairs of electrodes are shown in the optical image in Figure 2a. The gaps between the adjacent fingers of

the interdigitated electrodes were about 10 μm. Then, we used a focused ion beam (FIB) to mill trenches in Si/Si_3N_4 parallel to the electrodes, as shown in the optical image in Figure 2b; the locations of the trenches are indicated by the colored lines for clarity. We prepared trenches with various widths ranging from 200 nm to 2 μm; the distances between the trenches and the adjacent gold electrodes were no larger than 5 μm. We found that the bare substrate between the trench and the Cr/Au electrode is important for the success of the fabrication process, because the adhesion of MXene flakes is expected to be stronger to the hydrophilic plasma-treated Si_3N_4 than to hydrophobic gold. According to our experiments, the optimum value for the distance between the trench and the gold electrode was between 2 and 5 μm. With shorter distances, it was more likely to produce a non-uniform deposition of MXenes flakes on the substrate as well as to observe their strain and tearing. On the other hand, the longer distances required larger MXene flakes that could still reliably cover the trench, form good contact with the gold electrode, and cover the area in between.

Figure 2c illustrates the transfer procedure that we used to place the MXene flakes over the trenches. While this procedure also involves a PDMS stamp, as the previous reports,[22, 24, 32] it has several important modifications that helped to improve the transfer yield. When we originally reported the PDMS transfer method for making suspended $Ti_3C_2T_x$ membranes,[24] we deposited MXene flakes directly onto a PDMS stamp, which was then pressed against the substrate with prefabricated nanowells. Here, we introduced an additional step, in which the MXene flakes are first deposited on a clean Si/SiO_2 substrate. Deposition of MXene flakes on Si/SiO_2 had been tried in numerous studies in the past and is known to produce very flat and uniform flakes with minimal wrinkling,[22, 24-27] which can be explained by the fact that both $Ti_3C_2T_x$ and SiO_2 are hydrophilic and are maximizing their area of interaction. Also, $Ti_3C_2T_x$ MXene flakes are very well visible on

a silicon substrate with a 300-nm-thick layer of SiO_2.[26] As a result, it is possible to visually observe the coverage of MXene flakes on Si/SiO_2 and produce a sample with multiple isolated $Ti_3C_2T_x$ monolayers for the next fabrication step. An example of a Si/SiO_2 with a dense coverage of $Ti_3C_2T_x$ flakes can be seen in Figure 1d. If the MXene is directly deposited on a PDMS stamp, as we did previously,[24] the flakes are less visible and it is more difficult to control their density and uniformity for the following fabrication steps.

Then, the $Ti_3C_2T_x$ MXene flakes are transferred from a silicon substrate to a PDMS stamp. The flakes are unlikely to transfer just upon the contact because they have to transition from a hydrophilic Si/SiO_2 to a hydrophobic PDMS. However, a transfer could be accomplished if a microliter amount of deionized (DI) water is injected underneath the PDMS stamp with a micro-syringe (30 µl), see Figure 2c. The water molecules intercalate at the hydrophilic interface between the MXene flakes and the Si/SiO_2 substrate, significantly increasing the transfer yield onto the PDMS.

In the next step, a Si/Si_3N_4 substrate with a set of prefabricated electrodes and trenches is placed under the microscope on a homebuilt vacuum stage equipped with a heating sink (to keep the substrate in place and moderately heat it; see the inset in Figure 2c), the PDMS stamp is positioned over the trenches using an XYZ micromanipulator and gently pressed against the substrate. The XYZ manipulator is particularly useful if there is an interest in positioning a particular MXene flake over a particular trench in the substrate. However, in case of a high density of MXene flakes, as in the sample shown in Figure 1d, they could be nondeterministically stamped onto the substrate with trenches, and multiple suspended membranes would be stochastically produced. At this stage, the transfer yield can be increased by heating the substrate to 75 °C, which helps the flakes leave PDMS and transfer onto the Si/Si_3N_4. Without heating, the transfer yield

was lower and/or we had to exert extra pressure on the PDMS, resulting in wrinkled, sagged, or torn MXene flakes. The inset in Figure 2c shows an optical photograph of a homebuilt transfer setup with a heating stage.

Overall, the transfer process relies on controlling the hydrophobic and hydrophilic characteristics of the involved interfaces. We found that an oxygen plasma treatment of Si/SiO_2 and Si/Si_3N_4 substrates prior to the initial deposition and the final transfer of MXene flakes greatly improved the yield of the membranes. This can be rationalized by the fact that plasma treatment of Si/SiO_2 and Si/Si_3N_4 substrates increases the number of the surface hydroxyls[46] that can engage in hydrogen bonding the MXene functional groups,[38, 39] resulting in a stronger surface adhesion of $Ti_3C_2T_x$ flakes. In turn, stronger adhesion of the MXene flakes to Si/Si_3N_4 substrates prevents their sliding on the surface and sagging of membranes into the trenches, especially during the actuation.

Figure 3 demonstrates the results of a typical transfer process. Figure 3a shows SEM image of a large area of a Si/Si_3N_4 substrate with prefabricated interdigitated electrodes and trenches (this area is similar to the one shown in the optical photograph in Figure 2b before the transfer). Hundreds of MXene flakes have been successfully transferred onto this area, and many of them are suspended over the trenches in Si/Si_3N_4. The density of the MXene flakes is comparable to that shown for MXene flakes deposited on Si/SiO_2 (Figure 1d), demonstrating the high yield of the transfer, which we estimated to be around 95% for multiple experiments.

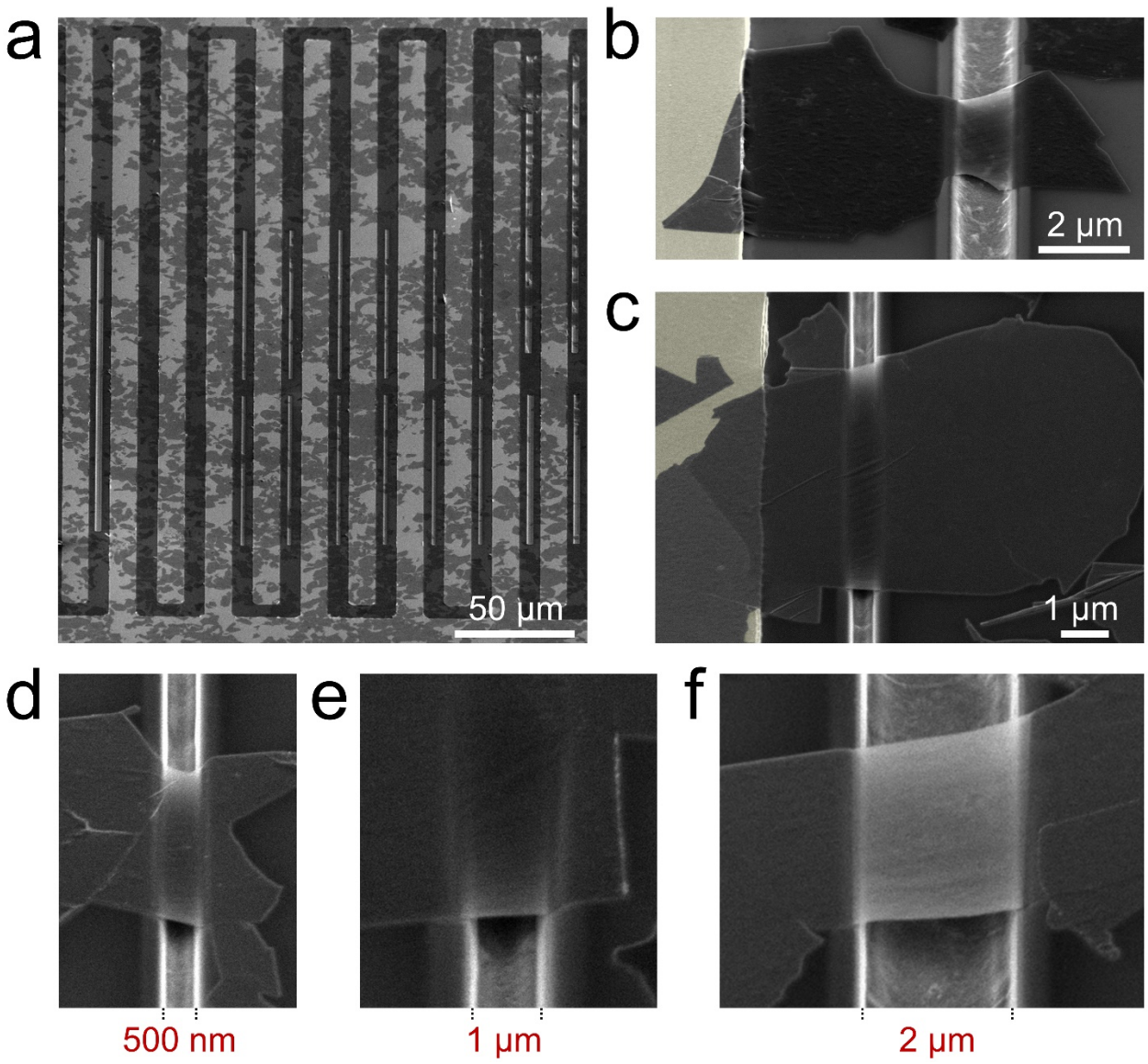

Figure 3. SEM images of $Ti_3C_2T_x$ MXene membranes over (a) large-scale interdigitated electrode-based NEMS devices and (b-f) four zoomed-in SEM images of membranes suspended over trenches with widths varying from 0.5 to 2 μm. In panels (b) and (c) the gold electrodes are highlighted in off yellow for clarity.

Figure 3b,c shows two representative MXene membranes that were formed as a result of this transfer. The membranes are very well stretched over the trenches and also contact the gold electrodes, which are highlighted in off yellow for clarity. The strong adhesion of the flakes to the plasma-treated Si/Si_3N_4 is illustrated by Figure 3b, which shows that the suspended membrane is not sagging despite a relatively small area of the flake on the right side of the trench. Because of the random shapes of the flakes, it is possible to find membranes with very different aspect ratios. Figure 3 also shows that it is possible to vary the trench width and suspend the MXene flakes over micrometer-scale distances. The trenches in Figure 3b and 3c have widths of 1.5 and 0.5 μm, respectively. In addition, Figure 3d-f shows same-magnification SEM images with three other membranes suspended over trenches with widths of 0.5, 1, and 2 μm. These images show representative structures, and on a large Si/Si_3N_4 substrate with multiple pairs of interdigitated electrodes (Figure 2a) hundreds of MXene membranes can be formed in a single transfer process.

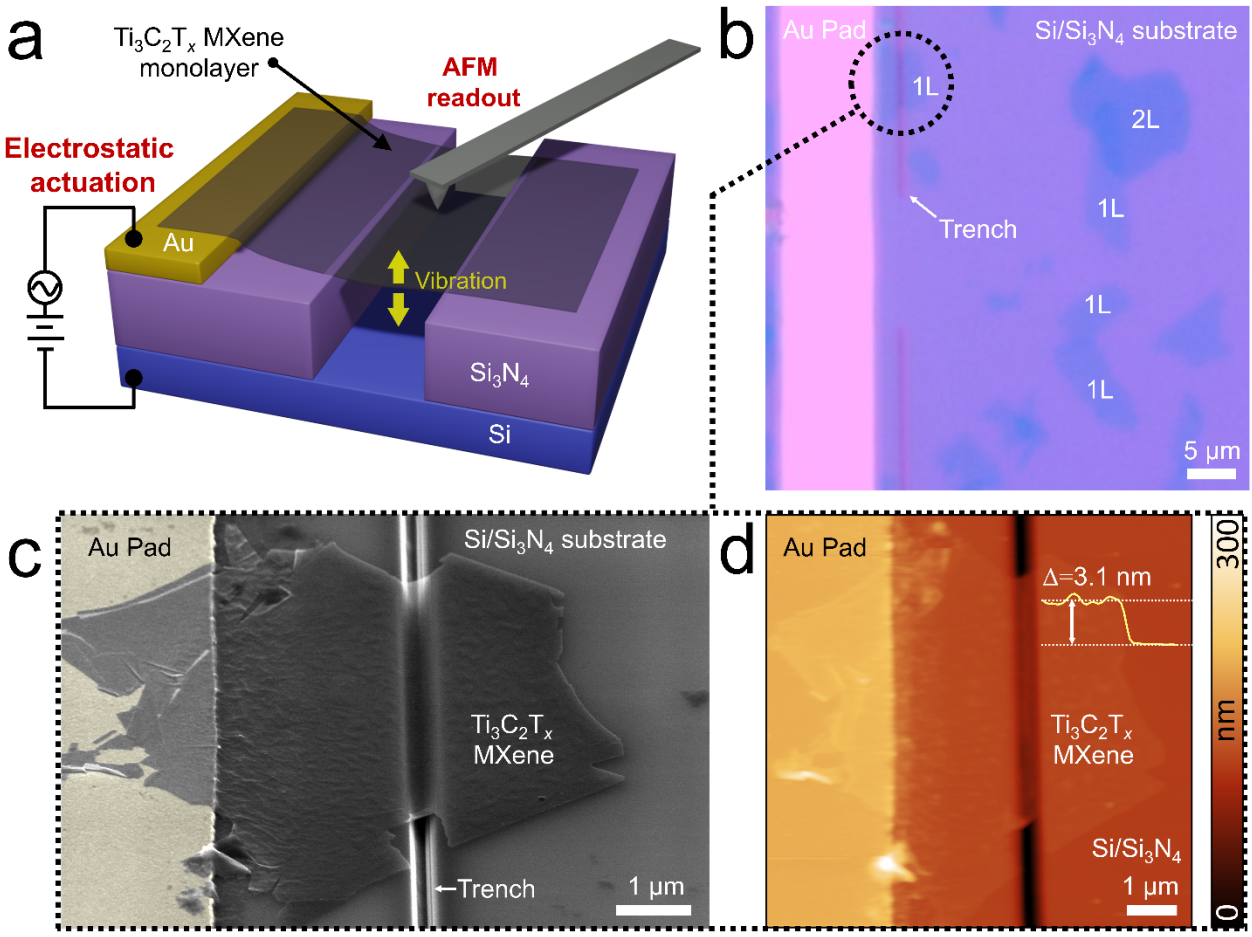

Figure 4. (a) Scheme of an electrostatically actuated $Ti_3C_2T_x$ MXene device probed by an AFM tip. (b) Optical image of the investigated MXene flake (in the circle) with several other deposited MXene flakes showing the difference between the monolayer (1L) and bilayer (2L) structures. (c) SEM image of a device based on a $Ti_3C_2T_x$ MXene flake that is connected to a gold pad and suspended over a trench that is about 400 nm wide. The gold electrode is highlighted in off yellow for clarity. The image was taken at an oblique angle relative to the surface. (d) AFM image of the same device as in panel (c) with an overlaid height profile recorded on the edge of the MXene flake.

Figure 4a shows a schematic representation of MXene-based devices that were fabricated and tested in this work. A monolayer $Ti_3C_2T_x$ MXene flake is suspended over a trench in a Si/ Si_3N_4 substrate and connected to a gold contact with a chromium underlayer. An AC voltage is applied between a gold pad and a conductive p-doped silicon substrate, resulting in an electrostatic actuation of a MXene membrane. The high electrical conductivity of $Ti_3C_2T_x$ MXene and a good electrical contact that it forms with gold electrodes[26, 27] are both important for this experimental design. The vertical displacement of the MXene membrane is recorded using an AFM tip.

Once $Ti_3C_2T_x$ MXene was transferred onto a substrate, a quick inspection with an optical microscope could be used to identify locations where the flakes are successfully suspended over the trenches and make contact with the gold electrode, as shown in Figure 4b. One of such locations with a $Ti_3C_2T_x$ MXene membrane is marked by a circle in Figure 4b. It should be noted that monolayer (1L), bilayer (2L), and thicker $Ti_3C_2T_x$ MXene flakes could be distinguished by optical microscopy on a Si/Si_3N_4 substrate. Figure 2b shows that the monolayer $Ti_3C_2T_x$ MXene looks different from the visibly darker bilayer flakes, which is very helpful for a quick determination of the thickness of the circled suspended flake that we identify as a monolayer. Although we also analyzed the thicknesses of the suspended MXene flakes by AFM, optical microscopy could be used for quick screening of monolayer membranes.

The circled MXene flake is also shown in the SEM image in Figure 4c, which was recorded at an oblique angle relative to the surface. The image shows that the membrane is well stretched over the trench and that there are no tears in the suspended portion of the flake. A large-area contact of the MXene flake with the gold electrode is also evident. In order to confirm that the $Ti_3C_2T_x$ flake in this device is a monolayer, we also performed its AFM analysis, see Figure 2d. The inset in Figure 4d shows that the flake has a thickness of about 3.1 nm, which is consistent with the values

that were previously reported for $Ti_3C_2T_x$ monolayers on Si/ Si_3N_4 substrates.[24, 26, 27] It should be noted that while the theoretical thickness of a $Ti_3C_2T_x$ monolayer is about 0.98 nm,[24] in the experimental AFM images, the monolayer $Ti_3C_2T_x$ flakes on Si/ Si_3N_4 appear much thicker, with thicknesses typically in the range of 2.5-3 nm. These values were rationalized by the presence of adsorbed molecules, such as water, as all those reported AFM measurements were performed in ambient conditions.[24, 26, 27] The AFM image in Figure 2d further shows that the MXene flake has a clean and uniform surface without visible contaminants or PDMS residues.

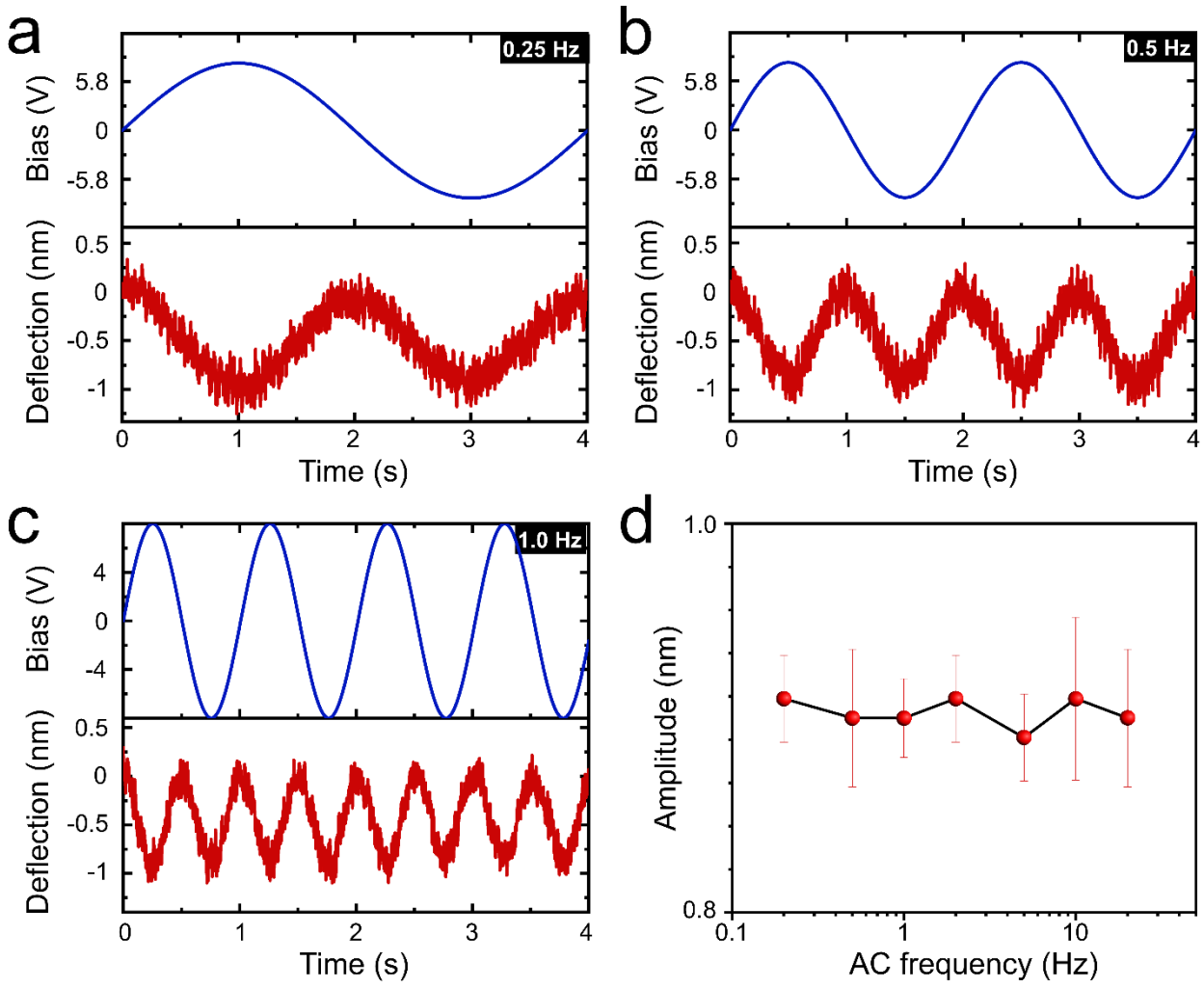

Figure 5. Electromechanical operation of a MXene device at different AC frequencies. The AC voltage wave had an amplitude of 8 V, and the vertical displacement of the suspended MXene flake was recorded using an AFM tip that applied a constant force of 2 nN to the membrane. The AC frequencies are (a) 0.25 Hz, (b) 0.5 Hz, and (c) 1 Hz. The blue curves show the AC voltage waveforms, while the red curves show the corresponding deflections of the MXene membrane. (d) Dependence of the membrane vibration amplitude for the same MXene device on AC frequency at the voltage amplitude of 8 V and the AFM tip loading force of 2 nN.

Figure 5 demonstrates the operation of the MXene device, which is shown in Figure 4b-d, at different AC frequencies. We applied a low-frequency AC voltage between the suspended MXene flake and the bottom electrode (p-doped Si), as shown in Figure 4a. First, we applied a sine wave that had an amplitude of 8 V and a frequency of 0.25 Hz, see Figure 5a. The AC voltage waveform is shown in the top panel, while the deflection of the center of the membrane relative to its unbiased position is shown in the bottom panel. As shown in Figure 4a, the deflection was recorded by an AFM tip, which applied a constant force of 2 nN to the membrane. The figure shows that the fabricated MXene device responds to the AC voltage and demonstrates periodic vibrations.

The electrostatic interaction between the MXene membrane and the bottom electrode is a result of the capacitive coupling when there is a potential mismatch, where the electrostatic force (F_{el}) is proportional to the capacitance gradient ($\partial C/\partial z$) and the square of the potential difference ($V_{ac}\cos\omega t$), *i.e.*, $F_{el} = 1/2\ \partial C/\partial z(V_{ac}\cos\omega t)^2$, and the AC component effective for the measurement is $F_{el} = 1/4\ \partial C/\partial z\ V_{ac}^2\cos 2\omega t$, so the membrane displacement amplitude is proportional to V_{ac}^2, and doubles the frequency of the AC voltage. In other words, regardless of whether the MXene sheet is charged positively and the substrate negatively or vice versa, the membrane always experiences an attractive electrostatic force toward the bottom of the trench. Thus, for each period of an AC voltage wave, the membrane has a maximum downward deflection twice, at both positive and negative AC voltage peaks. As a result, the deflection wave doubles the frequency of the AC voltage wave. During these experiments, the membrane displacement signal was reproducible, and we did not observe a signal degradation before the breakdown, *i.e.*, when the membrane was punched through by the AFM tip.

We tested this MXene device at different AC voltage frequencies and observed similar behavior to Figure 5a, see the data for the AC voltage frequencies of 0.5 Hz and 1 Hz in Figures

5b and 5c, respectively. In these measurements, we also used the AC voltage amplitude of 8 V and the AFM tip loading force of 2 nN. In all experiments, the device exhibited a periodic response to the AC voltage with a doubled frequency of vibrations. These tests also show that the MXene membrane exhibited the same amplitude of vibrations at different AC voltage frequencies, which is further illustrated by Figure 5d for the AC voltage frequency range from 0.25 to 20 Hz.

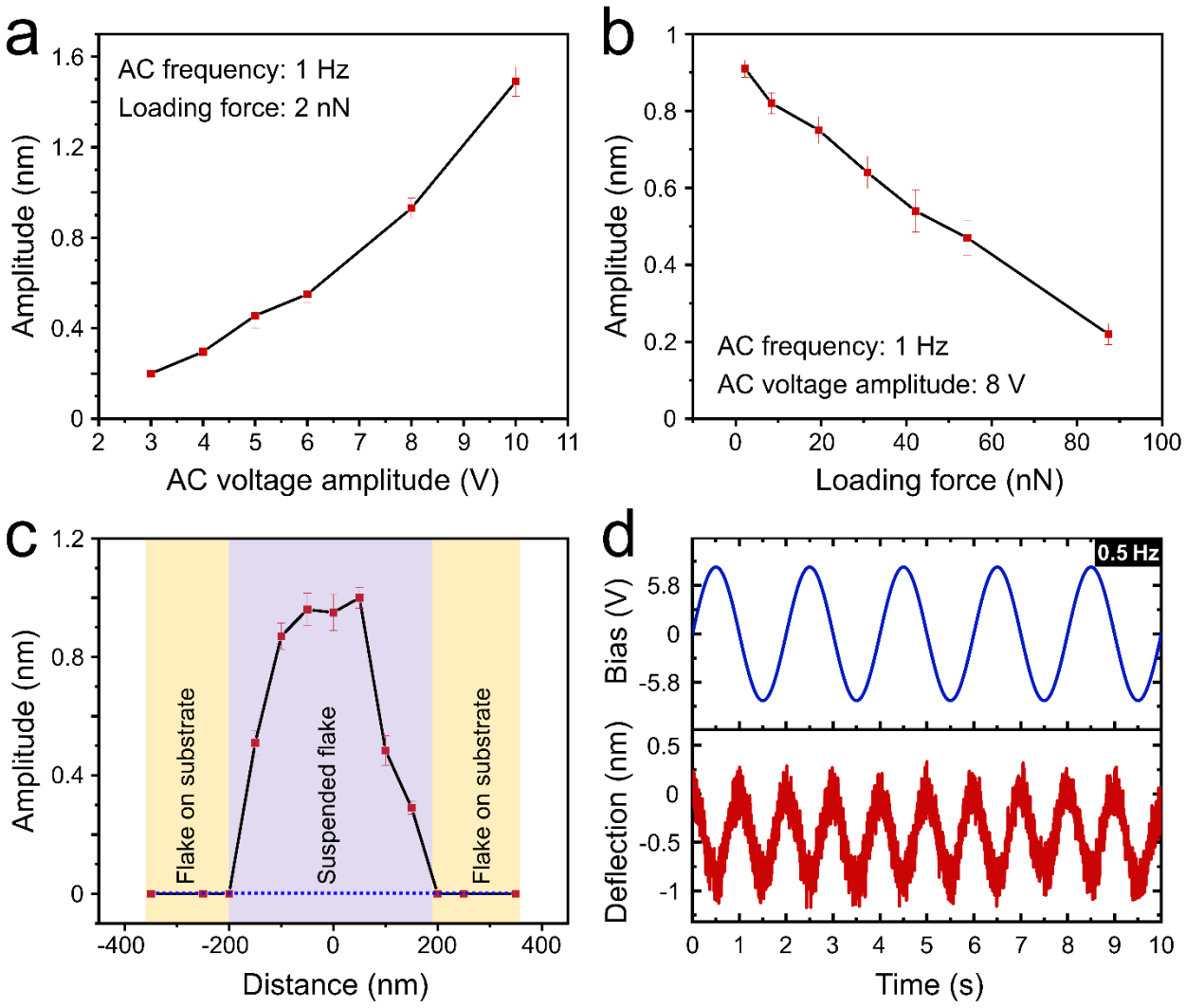

Figure 6. (a) Dependence of the membrane vibration amplitude on AC voltage amplitude at the AC frequency of 1 Hz and the AFM tip loading force of 2 nN. (b) Dependence of the membrane vibration amplitude on the AFM tip loading force at the AC frequency of 1 Hz and the voltage amplitude of 8 V. (c) Vibration amplitudes at different membrane positions across the trench at the AC frequency of 1 Hz, the voltage amplitude of 8 V, and the AFM tip loading force of 2 nN. (d) Cyclic electromechanical operation of the MXene device at the AC frequency of 0.5 Hz, the voltage amplitude of 8 V, and the AFM tip loading force of 2 nN.

The vibration amplitude of the MXene device can be tuned by the measurement parameters, such as the AC voltage amplitude (Figure 6a) and the AFM tip loading force (Figure 6b). Figure 4a shows that the vibration amplitude scales almost linearly with the AC voltage amplitude, increasing from about 0.2 nm at 3 V to about 1. 5 nm at 10 V. The vibration amplitude linearly decreases with the increasing loading force, as shown in Figure 6b. At the constant AC voltage amplitude of 8 V, which we used for most measurements, we observed a vibration amplitude of 0.91 nm at a 2 nN loading force, while it drops below 0.3 nm as the tip loading force increases up to 90 nN (Figure 6b). Thus, it is necessary to use large AC voltage amplitudes and small AFM tip-loading forces for large vibration amplitudes.

Since the vibrations were recorded with an AFM tip, it was possible to measure the displacement amplitudes at different membrane positions across the trench, see Figure 6c. The maximum displacement was measured close to the center of the suspended membrane, and no vibrations were observed for the flake on a substrate. Finally, the measurements were highly reproducible, as illustrated by Figure 6d, which shows multiple cycles of operation of the MXene device at an AC voltage amplitude of 8 V and a frequency of 0.5 Hz, and a 2 nN loading force. The experiments performed with other measurement parameters within the ranges shown in Figures 5d, 6a, and 6b revealed similarly reproducible cycles of operation of the device.

Furthermore, an estimation of the MXene membrane deflection amplitude, due to the electrostatic interactions based on the Euler–Bernoulli beam theory, can be expressed as $\delta = \frac{FL^3}{32Ewh^3}$, where δ is the maximum deflection of the membrane at the center of the trench, F is the uniformly distributed electrostatic force, L is the trench width, w is the membrane length over the trench, h is the thickness of the membrane, and E is the elasticity of the membrane. The electrostatic force estimated from the expression $F_{el} = 1/4\ \partial C/\partial z\ V_{ac}^2 \cos 2\omega t$ is about $F/w \sim 10^{-}$

^{3} N/m at 10 V V_{ac}. Substituting the numbers with $L \sim 400$ nm, $h \sim 1$ nm, and $E = 330$ GPa[24] yields an estimation of the free oscillation maximum deflection amplitude $\delta \sim 6$ nm at 10 V AC. In the actual experiments, the AFM tip is in contact with the membrane at a loading force of a few nN, which is considerably large compared to the electrostatic force, so the vibration is not entirely free and is suppressed by the AFM tip pressing. As a result, the experimental deflection amplitude is about a quarter of the value from the calculation, which also decreases when the AFM tip loading force increases.

3. Conclusions

In summary, we demonstrated the high-yield fabrication of suspended monolayer $Ti_3C_2T_x$ MXene flakes. The described procedure allows a transfer of hundreds MXene flakes onto a substrate with prefabricated electrodes and trenches, enabling preparation of numerous operational electromechanical devices based on monolayer MXene membranes on a single chip. The membranes are clean, uniform and well-stretched, and can be produced with various aspect ratios over trenches with gaps ranging from 200 nm to 2 μm. The devices reliably responded to the electrostatic actuation in ambient conditions over multiple cycles and with different measurement parameters, such as AC frequency, AC voltage amplitude, and AFM tip loading force. We believe that the successful fabrication and demonstration of electromechanical devices based on suspended $Ti_3C_2T_x$ membranes at the ultimate monolayer limit is an important step toward the exploration of the potential of MXenes for NEMS applications. It would be interesting to investigate these devices in a broader range of experimental conditions, as well as to explore different device geometries and $Ti_3C_2T_x$ flakes with different thicknesses. Furthermore, it would be very intriguing to explore practical applications of suspended $Ti_3C_2T_x$ monolayers in NEMS-based switches,

actuators, and sensors. Particularly promising is the recent report on $Ti_3C_2T_x$ resonators with a different geometry (a circular membrane) that were employed as mass sensors with zeptogram sensitivity.[32] For many practical applications, the AFM readout of membrane vibrations may not be optimal, and electrical and optical readout techniques could be explored for this purpose. Finally, while $Ti_3C_2T_x$ MXene has a great combination of properties for NEMS applications, such as a high electrical conductivity (>10,000 S cm^{-1})[26] and a high effective Young's modulus (~330 GPa),[24] other members of a very large family of MXenes[17, 18] should also be considered for studies on electromechanical actuation of suspended monolayer membranes, as some of them may reveal even better performance than $Ti_3C_2T_x$.

4. Experimental

4.1. Synthesis of Ti_3AlC_2 MAX phase

TiC (325 mesh), Al (325 mesh), and Ti (325 mesh) powders were purchased from Alfa Aesar. Ti, TiC, and Al were mixed at the molar ratio of 1:2:1.2 using a pestle and mortar, and the resulting mixture was annealed at 1400 ℃ for 4 h under the flow of argon (450 sccm). After the synthesis, the sample was crushed and washed with HCl (9M) for 6 h. After rinsing the sample with water (until pH 6 was reached) and drying under a vacuum, the powder sample was sieved, and particles in the range of 10-30 μm were used for the etching process.

4.2. Synthesis of $Ti_3C_2T_x$ MXene

Ti_3AlC_2 MAX phase (500 mg) was etched in a mixture of LiF (800 mg) and HCl (9M, 10 ml) for 24 h under ambient conditions. During the etching, the mixture was stirred at 500 rpm. The etched sample was gently washed with water until pH 6 was reached. Then, the washed sample was delaminated into flakes using a very gentle swirling.[37] The delaminated $Ti_3C_2T_x$ MXene sample was kept under nitrogen at 4 ℃ for further experiments.

4.3. Materials characterization

XRD patterns of Ti_3AlC_2 MAX phase and $Ti_3C_2T_x$ MXene powders were recorded using a PANalytical Empyrean diffractometer with Ni-filtered Cu K_α radiation operated at 40 kV and 30 mA. A step size of 0.03° and a 0.5 s dwelling time were used to collect the XRD patterns. Raman spectra of $Ti_3C_2T_x$ MXene flakes were collected using a Thermo Scientific DXR Raman microscope with a 532 nm excitation laser. Transmission electron microscopy (TEM) images and selected area electron diffraction (SAED) patterns were recorded using a FEI Tecnai Osiris instrument operated at 200 kV. For TEM imaging, the $Ti_3C_2T_x$ MXene flakes were deposited on a lacey carbon TEM grid. Scanning electron microscopy (SEM) of $Ti_3C_2T_x$ MXene flakes was performed using a FEI Nova NanoSEM 450 scanning electron microscope; the flakes were visualized on a Si/SiO_2 substrate.

4.4. Device fabrication

The MXene electromechanical actuators were fabricated on heavily p-doped Si substrates covered a 200-nm-thick Si_3N_4 (Silicon Quest International). The detailed fabrication steps are described below.

1. All substrates, including Si/SiO_2 and Si/Si_3N_4 were first plasma treated for 60 s (Plasmaetch PE-25, 400W 50KHz generator, USA). All substrates were kept in a clean container prior to use.
2. Interdigitated electrodes (Cr 5 nm/Au 45 nm) were patterned on a Si/Si_3N_4 substrate by the standard photolithography. Various patterns and geometries could be adopted depending on the experiment.
3. An AJA electron beam evaporation system with the standard operating procedure was used for the metal deposition.
4. Trenches with depths of about 200 nm and widths of 0.2-2 μm were fabricated near the Cr/Au electrodes by a gallium-focused ion beam (FIB) using a FEI Helios NanoLab 660 instrument. Standard procedure was used, and similar to step 2, various shapes and geometries can be adopted depending on the design and experiment purposes.

   It should be noted that it is important to optimize the FIB etching so that the depth of the trenches does not exceed the thickness of the Si_3N_4 layer. If the Si_3N_4 is overetched and the conductive Si layer is exposed at the bottom of the trenches, a MXene flake could sag into a trench and form a short between one of the Au pads and the silicon. A formation of such short would prevent the electrostatic operation of the fully suspended membranes employing the same Au pad as the top electrode.
5. A $Ti_3C_2T_x$ MXene solution with a concentration of 1 mg ml^{-1} was drop-casted on a plasma-treated Si/SiO_2 substrate and left for 60 s.
6. A cleanroom-grade tissue was used to remove excess water/solution from the substrate from step 5. The sample was left for 2 min to dry.

7. A modified PDMS water-assisted transfer method, which is illustrated by Figure 2, was used to transfer MXene flakes from Si/SiO_2 substrate onto Si/Si_3N_4 substrate. A 500 μm thick PDMS was used to transfer MXene flakes.
8. As shown in Figure 2c, the Si/SiO_2 substrate, with MXene flakes on it, was gently stamped with PDMS using an XYZ micromanipulator. The sample was left untouched for 30 s.
9. Using a microneedle, about 30 μl of DI water was injected under the PDMS layer to facilitate the transfer of MXene flakes onto the PDMS. The micromanipulator was moved along the Z axis to separate the PDMS from the Si/SiO_2 substrate.
10. The Si/Si_3N_4 substrate with a set of prefabricated electrodes and trenches was placed under the microscope on a homebuilt vacuum stage equipped with a heating sink (to keep the substrate in place and moderately heat it; see the inset of Figure 2c).
11. The PDMS stamp containing MXene flakes (from step 9) was positioned over the trenches using an XYZ micromanipulator and gently pressed against the substrate.
12. At this stage, the transfer yield can be significantly increased by heating the substrate to 75 °C for 120 s, which helps the flakes leave PDMS and transfer onto the Si/Si_3N_4,
13. The substrate with the suspended MXene flakes was kept in a clean container in a nitrogen-filled glove box for further experiments.

4.5. Device measurements

A commercial AFM system (MFP3D, Asylum Research) was used to detect the vertical vibrations of the MXene devices. An AC voltage was applied to a MXene membrane via a micromanipulator probe that was placed on a Cr/Au electrode connected to the membrane; the

conductive, heavily doped p-type silicon substrate served as the opposite electrode. An AFM tip with a non-conductive single-crystal diamond probe (D80, K-TEK Nanotechnology) was used as a sensor to pick up the vibration signal of the membrane. During the experiment, the AFM probe was brought in contact with the membrane at a low contact force of several nN, and the membrane vibration was transferred to the AFM tip, where the AFM cantilever deflection signal was recorded. The AFM cantilever optical lever sensitivity and spring constant were calibrated using built-in methods (*i.e.*, force-distance curves and thermal noise methods, respectively).

Conflicts of Interest

The authors declare no conflict of interest.

Acknowledgments

The work was supported by the Nebraska Center for Energy Sciences Research (NCESR) and the National Science Foundation (NSF) through EPSCoR RII Track-1: Emergent Quantum Materials and Technologies (EQUATE), award OIA-2044049. Some experiments were performed using the instrumentation at the Nebraska Nanoscale Facility, which is supported by the NSF (ECCS-2025298) and the Nebraska Research Initiative.

References

1. D. Akinwande, C. J. Brennan, J. S. Bunch, P. Egberts, J. R. Felts, H. Gao, R. Huang, J.-S. Kim, T. Li, Y. Li, K. M. Liechti, N. Lu, H. S. Park, E. J. Reed, P. Wang, B. I. Yakobson,

T. Zhang, Y.-W. Zhang, Y. Zhou and Y. Zhu, *Extreme Mechanics Letters*, 2017, **13**, 42-77.

2. K.-M. Hu, P. Bo, X.-Y. Li, Y.-H. Xin, X.-R. Bai, L. Li and W.-M. Zhang, *EPL (Europhysics Letters)*, 2020, **131**, 58001.
3. T. Yildirim, L. Zhang, G. P. Neupane, S. Chen, J. Zhang, H. Yan, M. M. Hasan, G. Yoshikawa and Y. Lu, *Nanoscale*, 2020, **12**, 22366-22385.
4. C. Lee, X. Wei, J. W. Kysar and J. Hone, *Science*, 2008, **321**, 385-388.
5. A. Falin, Q. Cai, E. J. G. Santos, D. Scullion, D. Qian, R. Zhang, Z. Yang, S. Huang, K. Watanabe, T. Taniguchi, M. R. Barnett, Y. Chen, R. S. Ruoff and L. H. Li, *Nat. Commun.*, 2017, **8**, 15815.
6. G. Fiori, F. Bonaccorso, G. Iannaccone, T. Palacios, D. Neumaier, A. Seabaugh, S. K. Banerjee and L. Colombo, *Nat. Nanotechnol.*, 2014, **9**, 768-779.
7. J. S. Bunch, A. M. van der Zande, S. S. Verbridge, I. W. Frank, D. M. Tanenbaum, J. M. Parpia, H. G. Craighead and P. L. McEuen, *Science*, 2007, **315**, 490-493.
8. C. Chen, S. Rosenblatt, K. I. Bolotin, W. Kalb, P. Kim, I. Kymissis, H. L. Stormer, T. F. Heinz and J. Hone, *Nat. Nanotechnol.*, 2009, **4**, 861-867.
9. X.-Q. Zheng, J. Lee and P. X. L. Feng, *Microsystems & Nanoengineering*, 2017, **3**, 17038.
10. J. Lee, Z. Wang, K. He, R. Yang, J. Shan and P. X.-L. Feng, *Science Advances*, 2018, **4**, eaao6653.
11. N. Morell, S. Tepsic, A. Reserbat-Plantey, A. Cepellotti, M. Manca, I. Epstein, A. Isacsson, X. Marie, F. Mauri and A. Bachtold, *Nano Lett.*, 2019, **19**, 3143-3150.

12. N. Morell, A. Reserbat-Plantey, I. Tsioutsios, K. G. Schädler, F. Dubin, F. H. L. Koppens and A. Bachtold, *Nano Lett.*, 2016, **16**, 5102-5108.

13. Z. Wang, H. Jia, X. Zheng, R. Yang, Z. Wang, G. J. Ye, X. H. Chen, J. Shan and P. X. L. Feng, *Nanoscale*, 2015, **7**, 877-884.

14. M. Will, M. Hamer, M. Müller, A. Noury, P. Weber, A. Bachtold, R. V. Gorbachev, C. Stampfer and J. Güttinger, *Nano Lett.*, 2017, **17**, 5950-5955.

15. S. Kim, J. Yu and A. M. van der Zande, *Nano Lett.*, 2018, **18**, 6686-6695.

16. F. Ye, A. Islam, T. Zhang and P. X. L. Feng, *Nano Lett.*, 2021, **21**, 5508-5515.

17. Y. Gogotsi and B. Anasori, *ACS Nano*, 2019, **13**, 8491-8494.

18. B. Anasori and Y. Gogotsi, *2D Metal Carbides and Nitrides (MXenes): Structure, Properties and Applications*, Springer International Publishing, 2019.

19. S. Bagheri, R. Chilcott, S. Luo and A. Sinitskii, *Langmuir*, 2022, **38**, 12924–12934.

20. M. Naguib, M. Kurtoglu, V. Presser, J. Lu, J. Niu, M. Heon, L. Hultman, Y. Gogotsi and M. W. Barsoum, *Adv. Mater.*, 2011, **23**, 4248-4253.

21. Y. Gogotsi and R. A. Andrievski, eds., *Materials Science of Carbides, Nitrides and Borides*, Kluwer, Dordrecht, NL, 1999.

22. A. Lipatov, M. Alhabeb, H. Lu, S. Zhao, M. J. Loes, N. S. Vorobeva, Y. Dall'Agnese, Y. Gao, A. Gruverman, Y. Gogotsi and A. Sinitskii, *Advanced Electronic Materials*, 2020, **6**, 1901382.

23. R. Chang and L. J. Graham, *Journal of Applied Physics*, 1966, **37**, 3778-3783.

24. A. Lipatov, H. Lu, M. Alhabeb, B. Anasori, A. Gruverman, Y. Gogotsi and A. Sinitskii, *Science Advances*, 2018, **4**, eaat0491.

25. A. Lipatov, M. J. Loes, N. S. Vorobeva, S. Bagheri, J. Abourahma, H. Chen, X. Hong, Y. Gogotsi and A. Sinitskii, *ACS Materials Letters*, 2021, **3**, 1088-1094.

26. A. Lipatov, A. Goad, M. J. Loes, N. S. Vorobeva, J. Abourahma, Y. Gogotsi and A. Sinitskii, *Matter*, 2021, **4**, 1413-1427.

27. A. Lipatov, M. Alhabeb, M. R. Lukatskaya, A. Boson, Y. Gogotsi and A. Sinitskii, *Advanced Electronic Materials*, 2016, **2**, 1600255.

28. A. Sarycheva, M. Shanmugasundaram, A. Krayev and Y. Gogotsi, *ACS Nano*, 2022, **16**, 6858-6865.

29. A. K. Geim, *Science*, 2009, **324**, 1530-1534.

30. Y. Huang, E. Sutter, N. N. Shi, J. Zheng, T. Yang, D. Englund, H.-J. Gao and P. Sutter, *ACS Nano*, 2015, **9**, 10612-10620.

31. A. Zobel, A. Boson, P. M. Wilson, D. S. Muratov, D. V. Kuznetsov and A. Sinitskii, *Journal of Materials Chemistry C*, 2016, **4**, 11081-11087.

32. D. Tan, X. Cao, J. Huang, Y. Peng, L. Zeng, Q. Guo, N. Sun, S. Bi, R. Ji and C. Jiang, *Advanced Science*, 2022, **9**, 2201443.

33. X. Du, I. Skachko, A. Barker and E. Y. Andrei, *Nat. Nanotechnol.*, 2008, **3**, 491-495.

34. K. I. Bolotin, K. J. Sikes, Z. Jiang, M. Klima, G. Fudenberg, J. Hone, P. Kim and H. L. Stormer, *Solid State Commun.*, 2008, **146**, 351-355.

35. A. A. Balandin, S. Ghosh, W. Bao, I. Calizo, D. Teweldebrhan, F. Miao and C. N. Lau, *Nano Lett.*, 2008, **8**, 902-907.

36. W. Bao, F. Miao, Z. Chen, H. Zhang, W. Jang, C. Dames and C. N. Lau, *Nat. Nanotechnol.*, 2009, **4**, 562.

37. M. Shekhirev, J. Busa, C. E. Shuck, A. Torres, S. Bagheri, A. Sinitskii and Y. Gogotsi, *ACS Nano*, 2022, **16**, 13695-13703.

38. J. Halim, K. M. Cook, M. Naguib, P. Eklund, Y. Gogotsi, J. Rosen and M. W. Barsoum, *Applied Surface Science*, 2016, **362**, 406-417.

39. M. Seredych, C. E. Shuck, D. Pinto, M. Alhabeb, E. Precetti, G. Deysher, B. Anasori, N. Kurra and Y. Gogotsi, *Chem. Mat.*, 2019, **31**, 3324-3332.

40. M. Alhabeb, K. Maleski, B. Anasori, P. Lelyukh, L. Clark, S. Sin and Y. Gogotsi, *Chem. Mat.*, 2017, **29**, 7633-7644.

41. A. Sarycheva and Y. Gogotsi, *Chem. Mat.*, 2020, **32**, 3480-3488.

42. D. B. Lioi, G. Neher, J. E. Heckler, T. Back, F. Mehmood, D. Nepal, R. Pachter, R. Vaia and W. J. Kennedy, *ACS Applied Nano Materials*, 2019, **2**, 6087-6091.

43. N. S. Vorobeva, S. Bagheri, A. Torres and A. Sinitskii, *Nanophotonics*, 2022, **11**, 3953-3960.

44. V. Presser, M. Naguib, L. Chaput, A. Togo, G. Hug and M. W. Barsoum, *Journal of Raman Spectroscopy*, 2012, **43**, 168-172.

45. H. Pazniak, I. A. Plugin, M. J. Loes, T. M. Inerbaev, I. N. Burmistrov, M. Gorshenkov, J. Polcak, A. S. Varezhnikov, M. Sommer, D. V. Kuznetsov, M. Bruns, F. S. Fedorov, N. S. Vorobeva, A. Sinitskii and V. V. Sysoev, *ACS Applied Nano Materials*, 2020, **3**, 3195-3204.

46. A. U. Alam, M. M. R. Howlader and M. J. Deen, *Journal of Micromechanics and Microengineering*, 2014, **24**, 035010.